Single-Scattering Albedo and Radiative Forcing of Various Aerosol Species with a Global Three-Dimensional Model

TOSHIHIKO TAKEMURA* AND TERUYUKI NAKAJIMA

Center for Climate System Research, University of Tokyo, Tokyo, Japan

OLEG DUBOVIK, BRENT N. HOLBEN, AND STEFAN KINNE

NASA Goddard Space Flight Center, Greenbelt, Maryland

(Manuscript received 11 January 2001, in final form 5 June 2001)

ABSTRACT

Global distributions of the aerosol optical thickness, Ångström exponent, and single-scattering albedo are simulated using an aerosol transport model coupled with an atmospheric general circulation model. All the main tropospheric aerosols are treated, that is, carbonaceous (organic and black carbons), sulfate, soil dust, and sea salt aerosols. The simulated total aerosol optical thickness, Ångström exponent, and single-scattering albedo for mixtures of four aerosol species are compared with observed values from both optical ground-based measurements and satellite remote sensing retrievals at dozens of locations including seasonal variations. The mean difference between the simulation and observations is found to be less than 30% for the optical thickness and less than 0.05 for the single-scattering albedo in most regions. The simulated single-scattering albedo over the Saharan region is, however, substantially smaller than the observation, though the standard optical constant of soil dust is used in this study. The radiative forcing by the direct effect of the main tropospheric aerosols is then estimated. The global annual mean values of the total direct radiative forcing of anthropogenic carbonaceous plus sulfate aerosols are calculated to be -0.19 and -0.75 W m^{-2} under whole-sky and clear-sky conditions at the tropopause, respectively.

1. Introduction

Anthropogenic and natural aerosols are recognized as significant atmospheric substances for the present and future climate changes (Houghton et al. 1996). They have two effects on the earth's radiation budget. One is a direct effect in which aerosol particles scatter and absorb the solar and thermal radiation. The other is an indirect effect in which they change the particle size and lifetime of cloud droplets acting as cloud condensation nuclei, leading to a cloud albedo change. There is, however, a large uncertainty in the evaluation of the aerosol radiative forcing due to a lack of our understanding of aerosol distributions and properties on a global scale because of their short lifetime of several days and the complicated variety of chemical components, emission sources, and size distributions. The optical properties and microphysical processes of cloud–aerosol interactions are also different among various aerosol species and hence are scarcely understood. The quantitative estimation of their effects, therefore, has been highly uncertain. According to the Houghton et al. (1996), the radiative forcing due to total anthropogenic aerosols was estimated to be -0.5 W m^{-2} with an uncertainty of a factor of 2 for the direct effect and over a wide range from 0 to -1.5 W m^{-2} for the indirect effect.

To estimate the past, present, and future climate forcings, a proper aerosol transport model is necessary for simulating the aerosol distributions. The three-dimensional distributions of sulfate aerosols have been simulated by many chemical transport models (e.g., Langner and Rodhe 1991; Chin et al. 1996), and the direct radiative forcing has also been estimated using their simulated distributions (e.g., Boucher and Anderson 1995; Feichter et al. 1997; Penner et al. 1998; Koch et al. 1999; Kiehl et al. 2000). There have also been several studies with three-dimensional models for carbonaceous aerosols (e.g., Liousse et al. 1996; Penner et al. 1998), and their direct and indirect effects on the climate system have recently been recognized as significant (Jacobson 2000; Ackerman et al. 2000). These models were mainly compared with measurements of surface con-

* *Current affiliation:* Research Institute for Applied Mechanics, Kyushu University, Fukuoka, Japan.

Corresponding author address: Teruyuki Nakajima, Center for Climate System Research, University of Tokyo, 4-6-1 Komaba, Meguroku, Tokyo 153-8904, Japan.
E-mail: teruyuki@ccsr.u-tokyo.ac.jp

centrations and several vertical profiles of each aerosol species. In recent years, on the other hand, global distributions of the aerosol optical thickness and Ångström exponent,[1] which are directly related to radiative transfer processes, have been retrieved from satellite- and ground-based remote sensing. For instance, Nakajima and Higurashi (1998) and Higurashi et al. (2000) analyzed the global distributions of the aerosol optical thickness and Ångström exponent including seasonal variations from the National Oceanic and Atmospheric Administration Advanced Very High Resolution Radiometer (AVHRR) radiance data using a two-channel method. The column-integrated aerosol spectral optical properties and size distributions have also been obtained from the ground-based observation network using the sun/sky photometer, Aerosol Robotic Network (AERONET), which has more than one hundred measurement sites (Holben et al. 1998, 2001). These observed column-integrated data on a global scale are very effective for examination of the simulated distribution of aerosol optical properties derived from aerosol transport models. To directly compare them, however, an aerosol model has to be developed for simulating the proper distributions of the total aerosol optical thickness by simultaneously treating all of the main aerosol species. Takemura et al. (2000) then developed a global three-dimensional aerosol transport model that treats main tropospheric aerosols, that is, carbonaceous [black carbon (BC) and organic carbon (OC)], sulfate, soil dust, and sea salt. The model was compared with not only measured aerosol surface concentrations but also with the optical thickness and Ångström exponent from AVHRR and AERONET retrievals.

In the radiative forcing estimation by an aerosol transport model, there is a further problem that produces a large bias caused by the improper assumptions of prescribed aerosol optical parameters even if the aerosol distributions are properly simulated. Even the sign of the direct radiative forcing can change when the atmosphere is loaded with aerosol species that significantly absorb the solar radiation, such as soil dust and BC. The inherent parameters for controlling the atmospheric shortwave absorption are the aerosol optical thickness, the single-scattering albedo for an optically thin atmosphere, and surface albedo (Yamamoto and Tanaka 1972). Although it is said that aerosols with a single-scattering albedo greater than 0.85 generally cool the planet, while those with less than 0.85 warm the planet (Hansen et al. 1981), there is a large variety in the reported values of the single-scattering albedo because of the large varieties in the chemical and physical structures of aerosols. Essentially, there have been few studies that showed the global distributions of the simulated aerosol single-scattering albedo and detailed comparisons of them with observations. Jacobson (2001) discussed the global/hemispheric and land/sea mean values of the simulated annual mean near-surface single-scattering albedo, which is compared at a few observational locations. In this study, therefore, we simulate the global distributions of the column-integrated aerosol single-scattering albedo with the aerosol transport model of Takemura et al. (2000) and compare them with various ground-based observations including seasonal variations over wide areas. The simultaneous treatment of various aerosol species in our simulation makes it possible to directly compare the simulated single-scattering albedo with the observed ones. The model is further used to calculate the aerosol direct radiative forcing. The model description is given in section 2. The features of the simulated optical thickness and Ångström exponent are summarized in section 3. The global distributions of the simulated single-scattering albedo are described in section 4, and they are also compared to observed data retrieved from AERONET (Dubovik and King 2000) and those obtained from other measurements. Section 5 discusses calculations of the direct radiative forcing for each aerosol species and mixing conditions of all the aerosol species. Our conclusions are presented in section 6.

2. Model description

The present model is an aerosol and chemical transport model coupled with the atmospheric general circulation model (AGCM) from the Center for Climate System Research (CCSR), University of Tokyo/National Institute for Environmental Studies (NIES), Tokyo, Japan. The basic dynamic and physical processes of the CCSR/NIES AGCM have been presented by Numaguti et al. (1995), and the radiation process modeling is described by Nakajima et al. (2000). The horizontal resolution of the triangular truncation is set at T42 (approximately 2.8° by 2.8° in lat and lon) and the vertical resolution at 11 layers (sigma level at 0.995, 0.980, 0.950, 0.900, 0.815, 0.679, 0.513, 0.348, 0.203, 0.092, and 0.021). The model time step is 20 min.

The main tropospheric aerosols, that is, carbonaceous (OC and BC), sulfate, soil dust, and sea salt, are treated in the present model. Carbonaceous aerosol sources are divided into the following six categories in this model: forest fires in tropical rain forests, those in other forests, fossil fuel consumption, fuel wood consumption, combustion of agricultural wastes, and the gas-to-particle conversion of terpene. In this model, the internal mixture of OC and BC is applied to the transport and radiation processes except that the 50% mass of BC originating from fossil fuel consumption is externally mixed. Ohta et al. (1996) and S. Ohta (2001, personal communication) indicated that the assumed external half mixture of BC presents the proper single-scattering albedo in the midlatitudes of the Northern Hemisphere. Jacobson (2000) suggested that the difference in the mixing condition makes a difference of ± 0.2 W m^{-2}

[1] Ångström exponent: The log-slope exponent of the spectral optical thickness between two wavelengths.

TABLE 1. Mass ratio of OC : BC for each source in the model.

Source	Forest fire (tropical)	Forest fire (other)	Fossil fuel	Fuel wood	Agriculture
OC/BC	8.28	6.92	3.33	5.64	6.92

in the direct radiative forcing of BC. The mass ratio of OC:BC is set to be different among sources according to Takemura et al. (2000; Table 1). Terpene changes to only OC. Precursor gases of sulfate aerosols are emitted from oceanic phytoplankton as dimethylsulfide (DMS), and fossil fuel consumption and volcanic activities as sulfur dioxide (SO_2). The aerosol transport processes include emission, advection, diffusion, and deposition. The advection scheme of large-scale transportation uses a flux-form grid method for aerosols and water vapor (A. Numaguti 1999, personal communication). To suppress numerical diffusion, the scheme adopts the fourth-order van Leer method (Lin et al. 1994), and the flux-form semi-Lagrangian method in polar regions (Lin and Rood 1996). The transportation by cumulus convection is also included in the present model. The sulfur chemistry is calculated using the three-dimensional monthly mean oxide fields of OH, H_2O_2, and ozone prescribed from the CCSR chemistry transport model (Sudo et al. 2000). The model can treat nudging of the meteorological parameters of wind, temperature, and specific humidity with reanalysis data. The present study uses the National Centers for Environmental Prediction–National Center for Atmospheric Research reanalysis data of 1990 for the nudged simulation to secure suitable accuracy for comparison with observations. The detailed explanation for aerosol emissions, transport processes, and sulfur chemistry has been described by Takemura et al. (2000).

Along with the total shortwave and longwave radiative flux calculation, the aerosol optical thicknesses at specific wavelengths of 0.55 and 1.0 μm are calculated at each time step to derive the optical thickness at the standard wavelength of 0.55 μm and the Ångström exponent defined as the log-slope exponent of the spectral optical thicknesses between the two wavelengths. The optical thickness τ is calculated using the extinction efficiency factor Q_{ext} at each wavelength λ and size bin i for soil dust and sea salt aerosols,

$$\tau(\lambda) = \sum_i \left(\frac{3}{4} \sum_{k=1}^{k_{\max}} \frac{Q_{\text{ext}}(\lambda, i) q_a(i, k) \Delta p_k}{\rho_a r_{\text{eff}}(i) g} \right), \quad (1)$$

where q_a is the aerosol mass mixing ratio at each size bin and the vertical model grid k, Δp_k is the pressure difference between the upper and lower boundaries at the kth layer, ρ_a is the aerosol particle density, r_{eff} is the aerosol effective radius at each size bin, and g is the gravitational constant. Tables 2 and 3 show the value of Q_{ext} of each size bin for soil dust and sea salt, respectively, used in the present model. In consideration of the hygroscopic growth, on the other hand, the mass extinction coefficient σ_m is given as a function of the relative humidity (RH) assuming a lognormal size distribution for carbonaceous and sulfate aerosols,

$$\tau(\lambda) = \sum_{k=1}^{k_{\max}} \frac{\sigma_m[\lambda, \text{RH}(k)] q_a(k) \Delta p_k}{g}. \quad (2)$$

The hygroscopic growth of aerosol particles is according to Tang and Munkelwitz (1994) for sulfate and Hobbs et al. (1997) for carbonaceous aerosols. Table 4 indicates σ_m of carbonaceous aerosols from savanna forest fires and that of sulfate aerosols with mode radii and standard deviations of the lognormal size distribution. The mass extinction coefficients of carbonaceous aerosols from other sources are variable depending on the mass radio of OC to BC. The mode radius and standard deviation of external and hydrophobic BC are set at 0.0118 and 2.3 μm, respectively. The optical thickness of absorption is also calculated with Eqs. (1) or (2) using the absorption efficiency factor or the mass absorption coefficient instead of Q_{ext} or σ_m, respectively. These optical parameters are calculated according to the Mie theory and volume-weighted refractive indices with water m for the internal mixture as follows:

$$m(\lambda) = m_w(\lambda) + [m_o(\lambda) - m_w(\lambda)] \left(\frac{r_o}{r_a(\text{RH})} \right), \quad (3)$$

where m_w and m_o are the refractive indices of water and dry aerosols according to d'Almeida et al. (1991) and WCP-55 (1983), respectively; r_o and r_a are the radii of dry and water-absorbing particles, respectively. The refractive index of internally mixed carbonaceous aerosols composed of OC and BC is calculated in the same way as in Eq. (3). These prescribed optical parameters and

TABLE 3. Extinction efficiency factor Q_{ext} of sea salt aerosols at 0.55 and 1.0 μm for the effective radius r_{eff} of each size bin in the model.

r_{eff} (μm)	0.18	0.56	1.78	5.62
Q_{ext} (0.55 μm)	1.04	3.81	2.16	2.27
Q_{ext} (1.0 μm)	0.17	2.74	1.99	2.00

TABLE 2. Extinction efficiency factor Q_{ext} of soil dust aerosols at 0.55 and 1.0 μm for the effective radius r_{eff} of each size bin in the model.

r_{eff} (μm)	0.13	0.20	0.33	0.52	0.82	1.27	2.02	3.20	5.06	8.02
Q_{ext} (0.55 μm)	0.86	2.38	4.10	2.59	2.73	2.28	2.34	2.11	2.17	2.09
Q_{ext} (1.0 μm)	0.13	0.52	2.06	3.74	3.57	2.07	2.10	2.07	2.09	2.10

TABLE 4. Mass extinction coefficient σ_m of carbonaceous aerosols from savanna forest fires and that of sulfate aerosols for each mode radius r_m depending on the relative humidity at 0.55 and 1.0 μm in the model.

	Relative humidity (%)							
	0	50	70	80	90	95	98	99
Carbonaceous (std dev = 1.80)								
r_m (μm)	0.100	0.108	0.110	0.144	0.169	0.196	0.274	0.312
σ_m (0.55 μm, m^2 g^{-1})	4.63	5.78	6.09	13.36	21.09	30.91	58.41	61.57
σ_m (1.0 μm, m^2 g^{-1})	1.42	1.75	1.84	4.77	8.32	14.38	46.74	69.93
Sulfate (std dev = 2.03)								
r_m (μm)	0.070	0.085	0.095	0.103	0.122	0.157	0.195	0.231
σ_m (0.55 μm, m^2 g^{-1})	4.28	7.21	10.12	12.60	20.09	35.04	44.95	47.38
σ_m (1.0 μm, m^2 g^{-1})	0.98	2.08	3.29	4.48	8.05	20.36	42.01	69.51

size distributions of dry particles as well as the prescribed internal and external mixture methods can create some errors in calculations of the aerosol optical thickness, single-scattering albedo, and radiative forcing as in other aerosol models. In this study, however, we try to tune the associated model parameters so as to produce good agreement with observed aerosol optical thickness and single-scattering albedo as shown in section 3 and 4.

The radiative process in the CCSR/NIES AGCM is calculated every 3 h by the two-stream discrete ordinate/adding method and by a *k*-distribution method for gas absorption due to H_2O, CO_2, O_2, O_3, N_2O, CH_4, and clorofluorocarbons (Nakajima et al. 2000). The spectral resolution for broadband flux calculations is 8 bands for the solar region and 10 for the thermal region. Size distributions, hygroscopic growth rates, and mode radii are the same in the separate spectral calculation of the optical thickness at 0.55 and 1.0 μm for carbonaceous and sulfate aerosols. The broadband calculation for total shortwave and longwave fluxes assumes the volume mode radius and standard deviation of the lognormal size distribution to be 4.0 and 2.5 μm, respectively, for soil dust instead of dividing into size bins. The mode radius of sea salt changes depending on the surface wind velocity [Takemura et al. 2000, Eq. (6)] and the standard deviation is set at 2.51 with the lognormal distribution. Figure 1 shows the spectral mass extinction coefficient and single-scattering albedo for dry particles of each aerosol species used in the present model. Extinction efficiencies of small particles, such as carbonaceous, externally mixed black carbon, and sulfate aerosols, decrease with the wavelength. On the other hand, those of soil dust and sea salt are almost constant in the solar bands. The Ångström exponent is therefore smaller for soil dust and sea salt than for other aerosol species. It is found from Fig. 1b that sulfate and sea salt aerosols scatter the solar radiation without significant absorption and that soil dust, carbonaceous, and externally mixed black carbon absorb both the solar and thermal radiation. The mass extinction coefficient and single-scattering albedo of liquid water are also shown in Fig. 1. A lognormal size distribution is also assumed for a liquid water cloud with a volume mode radius of 8.0 μm and a standard deviation of 1.5.

Aerosol direct radiative forcings at the surface and each vertical boundary are calculated as the difference in net fluxes with and without aerosols under the same meteorological conditions. In this calculation, there are

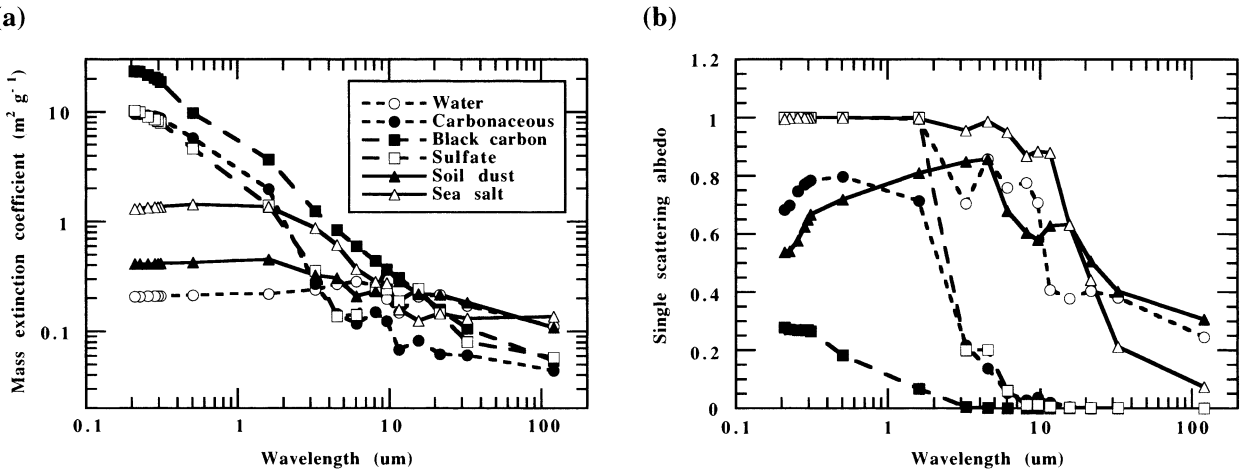

FIG. 1. Spectra of (a) the mass extinction coefficient and (b) the single-scattering albedo of each aerosol species for dry particles and the cloud water droplet assumed in the present model.

aerosol particles both in clear and cloudy regions. The mass ratio of internally mixed aerosols in cloud water is assumed to be 0.1 for soil dust and BC, 0.3 for carbonaceous and sulfate, and 0.6 for sea salt aerosols in cloudy regions. The extinction and absorption efficiencies of cloud droplets are variable with the internal mixture of aerosol particles. These ratios are also assumed for the in-cloud coefficients used in the wet deposition process [Takemura et al. 2000, Eq. (A8)].

3. Aerosol optical thickness and Ångström exponent

Figure 2 shows the simulated seasonal mean distributions of the aerosol optical thickness at a wavelength of 0.55 μm and the Ångström exponent for the mixed polydispersion of carbonaceous, sulfate, soil dust, and sea salt. Saharan dust particles are transported to the subtropical Atlantic by the trade wind throughout the year with a large optical thickness and a small Ångström exponent from 0 to 0.4. Large optical thickness values are also seen in the Arabian region, especially in the Northern Hemisphere summer, which can be explained by monsoon wind transportation of Arabian dust. Another prominent contributor to the optical thickness is carbonaceous aerosols with a large Ångström exponent over 1.0 originating from biomass burning over central Africa in the Northern Hemisphere winter and the Amazon and southern Africa in the latter half of the year. The simulated Ångström exponent is large over land of these biomass-burning regions even in wet seasons because of the gas-to-particle conversion of terpene, though the optical thickness is small. There is a large column loading of anthropogenic aerosols, such as sulfate and carbonaceous, originating mainly from fossil fuel and domestic fuel consumptions over east and south Asia, North America, and Europe with large Ångström exponent values. The enhancement of the optical thickness over the midlatitudes of the Northern Hemisphere in summer is partly caused by hygroscopic growth with high relative humidity, leading to an increase in the extinction efficiency. Other reasons are fast oxidation of SO_2 and DMS due to high temperature, high oxide concentrations, and strong vertical convection due to instability of the atmosphere in summertime.

These simulated seasonal and geographical patterns of aerosol distributions are consistent with the AVHRR retrieval (Higurashi et al. 2000). Monthly mean values of the optical thickness and Ångström exponent calculated in this model are compared quantitatively with AERONET retrievals (Holben et al. 1998, 2001) in Fig. 3. These simulated optical parameters have become closer to the observed values than those by the old version of this model given by Takemura et al. (2000) because of an improvement in the optical treatments and the finer model grid from T21 to T42. Seasonal variations in the simulated and observed optical thicknesses are in good agreement and seasonal mean biases are less than 30% at most sites. Over the United States, the optical thickness is high in summer for both the simulation and observation (Figs. 3a and 3b). On the other hand, Europe has large optical thicknesses from spring to summer (Figs. 3c and 3d). The small optical thickness around or less than 0.1 is reproduced well by the model over remote ocean areas (Figs. 3e and 3f). Over the dominant regions of Saharan dust particles, the simulated optical thickness is close to AERONET retrievals including seasonal variations (Figs. 3g–j). AERONET detects the contrast in optical thickness values between dry and wet seasons over southern Africa and South America due to biomass burning (Figs. 3k and 3l). Although this contrast is simulated well, the temporal difference between simulated and AERONET optical thicknesses by one or two months may be caused by the prescribed monthly emission data on biomass burning and the difference between simulated and observed years. The simulated result shows a characteristic distribution pattern of large Ångström exponent values in biomass-burning and industrial regions, small values in soil dust regions, and intermediate values between them in the remote ocean, of which patterns are also observed by the AERONET results. The agreement is particularly good with the AERONET values in the midlatitudes of the Northern Hemisphere, the remote oceans, and biomass-burning regions during the dry season, though the simulated values overestimate the observed values in dust regions.

4. Single-scattering albedo

a. Global distribution of simulated single-scattering albedo

Figure 4 shows the simulated seasonal mean distributions of the column-integrated aerosol single-scattering albedo for a mixed polydispersion of carbonaceous, sulfate, soil dust, and sea salt at 0.55 μm. Saharan and Arabian dust particles make the single-scattering albedo as small as 0.8–0.9 because of the strong absorption of the direct solar radiation and the reflected radiation caused by bright surfaces. Especially, the strong ultraviolet absorption of the desert soil aerosols is detected by the total ozone mapping spectrometer (TOMS) (Herman et al. 1997). The single-scattering albedo is also low over the Gobi and Takla Makan Deserts because of Asian dust generated in the present model. Biomass burning emits not only OC and sulfate aerosols but also BC, so that the single-scattering albedo is calculated to be as low as 0.85 over southern Africa and the Amazon in the dry season. Over industrial regions, such as east Asia, Europe, and North America, the single-scattering albedo is simulated to be about 0.9 due to large contributions of sulfate, OC, and BC. A slightly smaller value of the simulated single-scattering albedo is seen in spring than in other seasons over the arctic region, which is observed as arctic haze (Heintzenberg and Leck

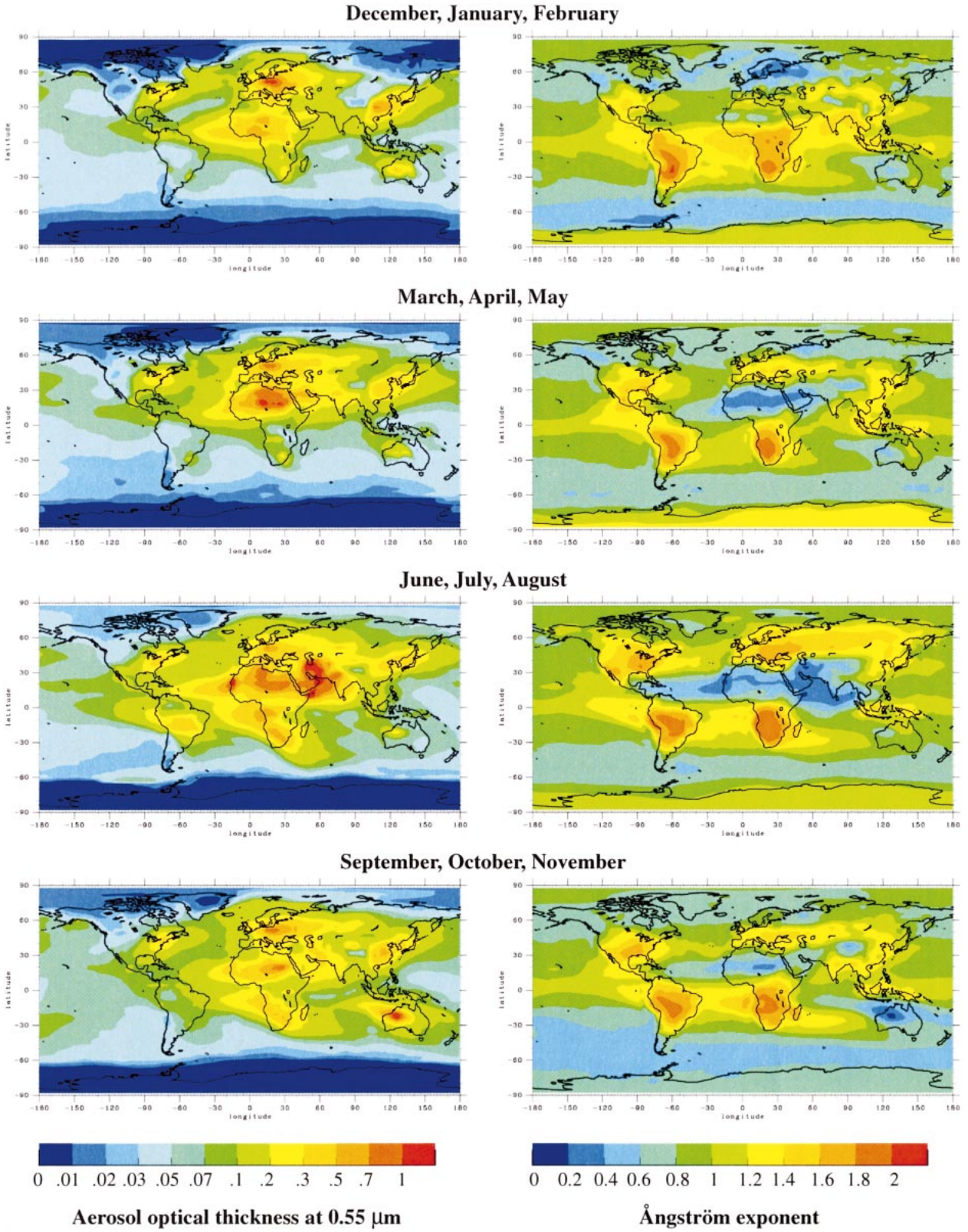

FIG. 2. Seasonal mean distributions of the simulated optical thickness at 0.55 μm (left) and the Ångström exponent (right) for a mixed polydispersion of all aerosol species, i.e., carbonaceous (OC and BC), sulfate, soil dust, and sea salt.

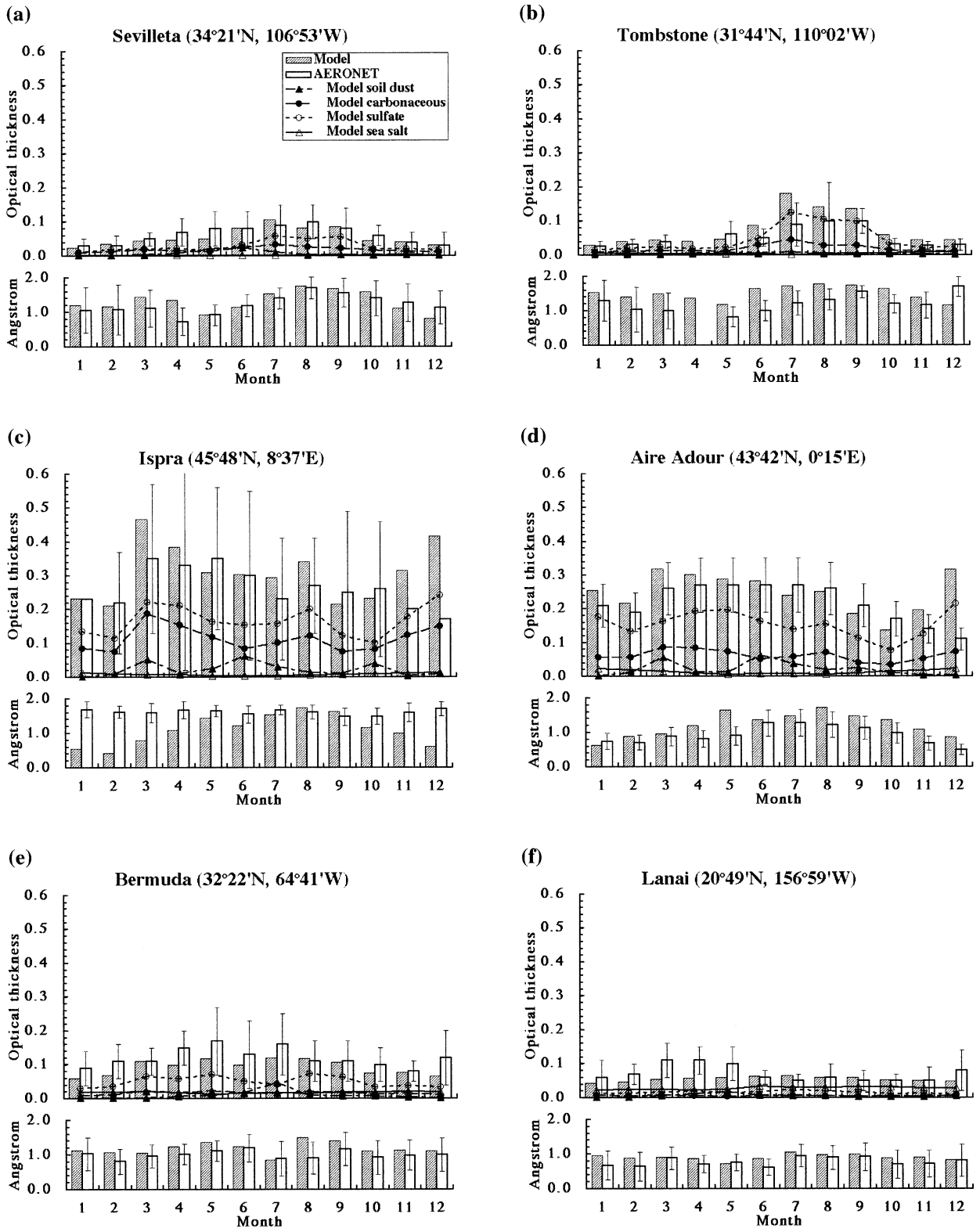

FIG. 3. Comparisons of the monthly mean simulated optical thickness and Ångström exponent for the mixture of all aerosol species, i.e., carbonaceous (OC and BC), sulfate, soil dust, and sea salt, with AERONET retrievals (columns) at 12 locations. Plots also show the simulated optical thickness for each aerosol component.

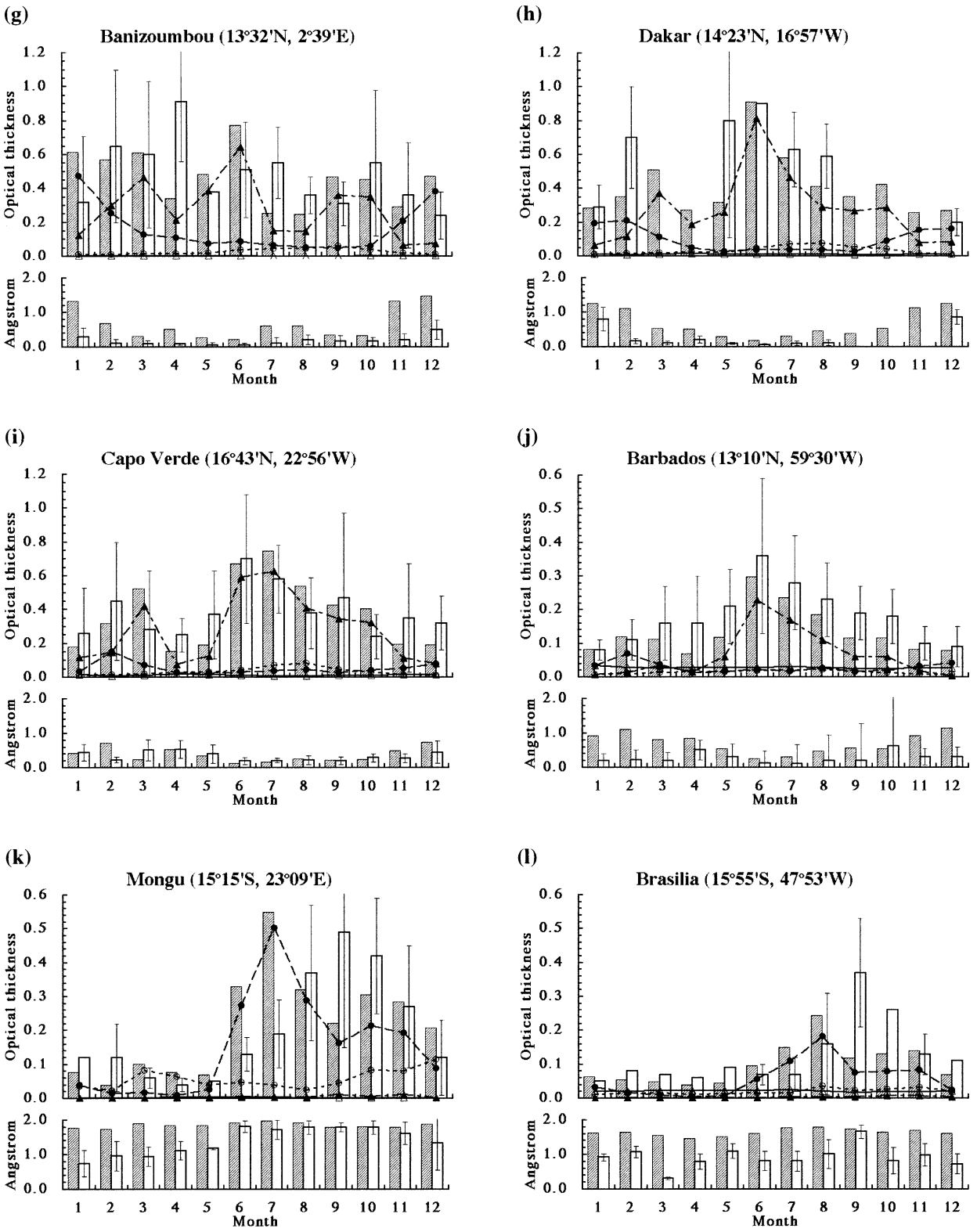

FIG. 3. (*Continued*)

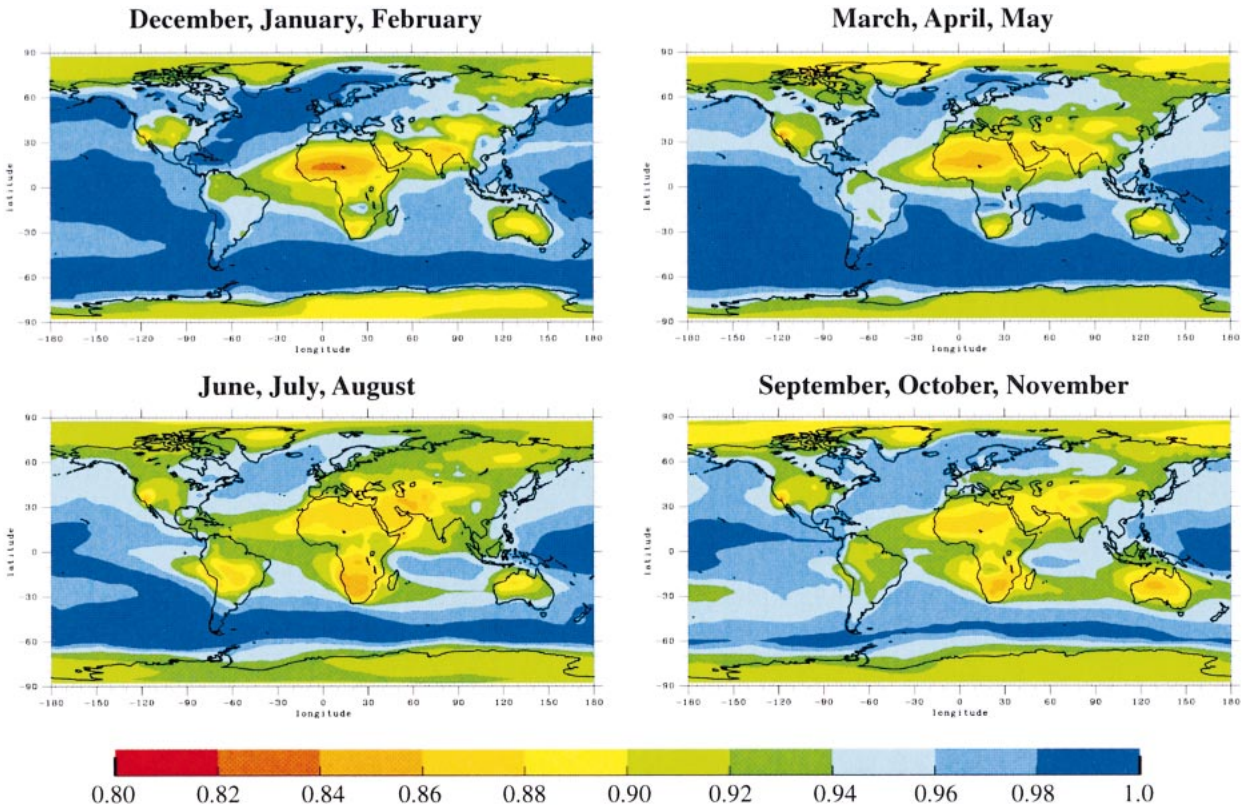

FIG. 4. Seasonal mean distributions of the simulated single-scattering albedo at 0.55 μm.

1994). This small single-scattering albedo is caused by transportation of BC from industrial regions in the mid- and high-latitudes of the Northern Hemisphere. Over the remote oceans, especially in the Southern Hemisphere, the single-scattering albedo is simulated to be close to 1.0 by domination of nonabsorbing aerosols such as sea salt and sulfate aerosols.

b. Comparisons with AERONET and other observations

Recently, the single-scattering albedo of column-integrated aerosols has started to be obtained from optical observations. AERONET provides quality-assured data for aerosol optical properties measured by the sun/sky multiwavelength radiometer at over 100 sites (Holben et al. 1998, 2001; Dubovik and King 2000). They are useful to test the results simulated by the present model, though it is suggested that the single-scattering albedo retrieved from AERONET can include some biases and errors (Dubovik et al. 2000; Smirnov et al. 2000). Jacobson (2001) showed a modeled annual mean value of the near-surface single-scattering albedo and compared it with several in situ observations. In this study, on the other hand, the column-integrated single-scattering albedos derived from the present model and AERONET are compared using monthly mean values at dozens of locations. The representative sites are selected as shown in Fig. 5. The AERONET retrieval is performed at four wavelengths—0.44, 0.67, 0.87, and 1.02 μm, and the single-scattering albedo at 0.55 μm is obtained by interpolation between 0.44 and 0.67 μm. The uncertainty of the single-scattering albedo retrieved by AERONET is within 0.03 for high aerosol loading with an optical thickness at 0.44 μm higher than 0.5, while it increases to 0.05–0.07 for lower aerosol optical thicknesses (Dubovik et al. 2000). The uncertainty of the AERONET retrieval is shown as error bars in Fig. 5.

Both the simulated and AERONET single-scattering albedos are similar to or slightly larger than 0.9 over the United States with small seasonal variations (Figs. 5a–d). There is sometimes a difference, on the other hand, between simulated and AERONET single-scattering albedos in the case of a small aerosol optical thickness (Fig. 5d). This might be because the confidence level of the AERONET retrieval becomes significantly low for the low optical thickness. In northern Italy (Fig. 5e), the single-scattering albedo is over 0.9 as well as over the United States both in the simulation and observation. At Kaashidhoo (Fig. 5f), which is an island off southern India, both simulated and AERONET values of the single-scattering albedo are around 0.9, which is close to values over industrial regions such as the United States and Europe. It is pointed out in the Indian Ocean Experiments (INDOEX) that not only sul-

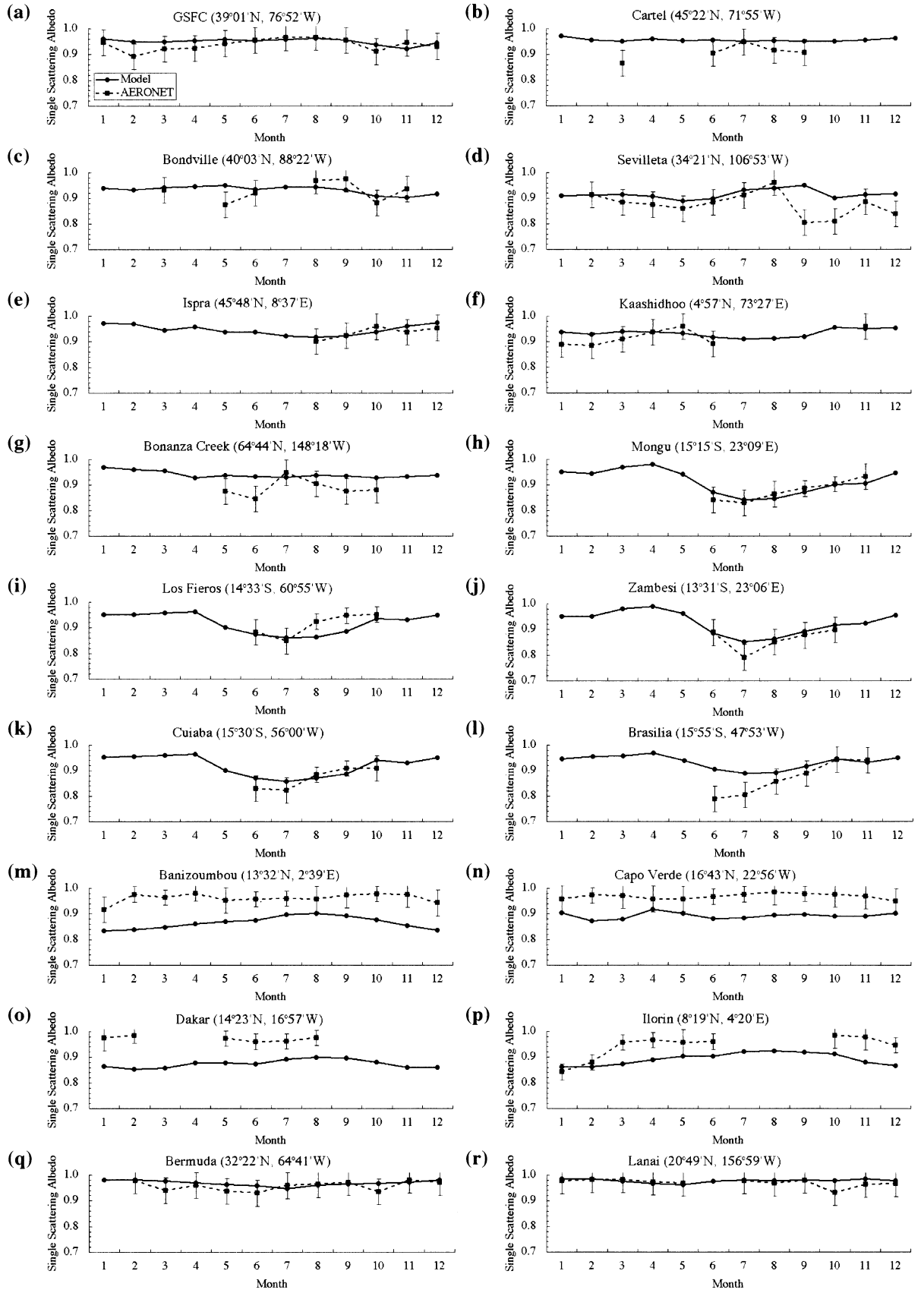
(a)
GSFC (39°01'N, 76°52'W)
(b)
Cartel (45°22'N, 71°55'W)
(c)
Bondville (40°03'N, 88°22'W)
(d)
Sevilleta (34°21'N, 106°53'W)
(e)
Ispra (45°48'N, 8°37'E)
(f)
Kaashidhoo (4°57'N, 73°27'E)
(g)
Bonanza Creek (64°44'N, 148°18'W)
(h)
Mongu (15°15'S, 23°09'E)
(i)
Los Fieros (14°33'S, 60°55'W)
(j)
Zambesi (13°31'S, 23°06'E)
(k)
Cuiaba (15°30'S, 56°00'W)
(l)
Brasilia (15°55'S, 47°53'W)
(m)
Banizoumbou (13°32'N, 2°39'E)
(n)
Capo Verde (16°43'N, 22°56'W)
(o)
Dakar (14°23'N, 16°57'W)
(p)
Ilorin (8°19'N, 4°20'E)
(q)
Bermuda (32°22'N, 64°41'W)
(r)
Lanai (20°49'N, 156°59'W)
Model
AERONET
Single Scattering Albedo
Month

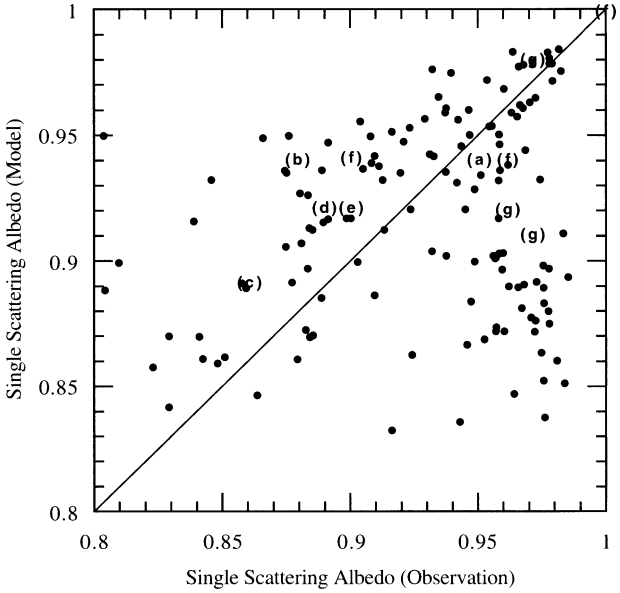

FIG. 6. Scatterplot of the simulated single-scattering albedo vs AERONET (dot) and other (alphabet) observations. References are (a) Nakajima et al. (1989), (b) Tanaka et al. (1990), (c) Qiu et al. (1987), (d) Ohta et al. (1996), (e) Kaufman et al. (1992), (f) Clarke (1989), and (g) Bodhaine (1995).

fate and organics but also soot are transported from south Asia to this area (Satheesh and Ramanathan 2000). The single-scattering albedo is close to 0.9 also over the high latitudes of the Northern Hemisphere (Fig. 5g) due to outflow of anthropogenic aerosols from the mid-latitudes.

Over southern Africa and the Amazon (Figs. 5h–l), seasonal variations are in good agreement between simulated and observed single-scattering albedos. The values are from 0.8 to 0.9 in the dry season due to biomass burning and over 0.9 in the wet season. Low single-scattering albedo during the dry season was also observed in the Smoke, Clouds, and Radiation-Brazil Project (SCAR-B) experiment (Hobbs et al. 1997). There is a large difference in Brasilia between simulated and observed values in June and July because AERONET may detect local pollution by urban activities (Fig. 5l).

Over northern Africa (Figs. 5m–p) where the dominant aerosol species is soil dust, the single-scattering albedo is almost less than 0.9 in the simulation but around 0.95 in AERONET that is close to values in clean regions. It is known that Saharan dust contains a large amount of hematite that is a reddish mineral composed of iron oxide that strongly absorbs both solar and infrared radiation (Quijano et al. 2000). The single-scattering albedo of hematite is calculated to be 0.65 at wavelengths from 0.2 to 0.6 μm (Sokolik and Toon 1999). In this study, the spectral single-scattering albedo of soil dust is set to be similar to the definition of Saharan dust in Quijano et al. (2000) as shown in Fig. 1b. On the other hand, Carlson and Benjamin (1980) calculated the value of the single-scattering albedo to be 0.86 at 0.53 μm using the refractive index determined from several measurements. This uncertainty of the single-scattering albedo in desert regions shows the necessity of further investigations for the optical properties of soil dust. Over the coast of the Gulf of Guinea (Fig. 5p), however, both simulated and AERONET single-scattering albedos are in good agreement in the dry season (January and February) because of the mixture of biomass-burning aerosols with soil dust. Single-scattering albedo values over the remote oceans of the northern Atlantic and the northern Pacific (Figs. 5q and 5r) are about 0.95 through the year for both the simulation and observations.

Figure 6 summarizes comparisons of the simulated single-scattering albedo with measured values of AERONET and other observations. Nakajima et al. (1989) compared aerosol optical properties between normal and Asian dust event conditions. The single-scattering albedo in the normal condition is as large as 0.95 in Nagasaki which is a midsize city in Japan with a population of a half million. Tanaka et al. (1990) carried out aircraft measurements using an aureolemeter over Nagoya, a typical urban area in Japan with a population of two million, for which the observed value is as low as 0.88. The value obtained by Qiu et al. (1987) is further as small as 0.86 in Beijing, China. They pointed out that the major source of aerosol pollution in winter is coal combustion in Beijing. The variety in the reported values is consistent with the amount of soot particle emission in each city. Ohta et al. (1996) indicated that the state of the mixture, such as internal or external mixtures of aerosol particles, is also important to determine the aerosol single-scattering albedo. They calculated the single-scattering albedo based on their observations in a range from 0.90 to 0.96 for an external mixture and from 0.85 to 0.93 for an internal half mixture of elemental carbon and sulfate aerosols under the free atmosphere condition. Kaufman et al. (1992) retrieved a single-scattering albedo of 0.9 from an aircraft measurement in the Biomass Burning Airborne and Spaceborne Experiment in the Amazonas (BASE-A) in September 1989. The observed single-scattering albedo from the shipborne measurement in the Soviet-American Gas and Aerosol Experiment (SAGA II) in 1987 ranges from 0.9 to 1 (Clarke 1989). Kamchatka, Russia, and Singapore results show small values indicating the effects of industrial and biomass-burning aerosols,

←

FIG. 5. Comparisons of monthly mean values of the simulated (solid line) and AERONET (dashed line) single-scattering albedos at 18 locations.

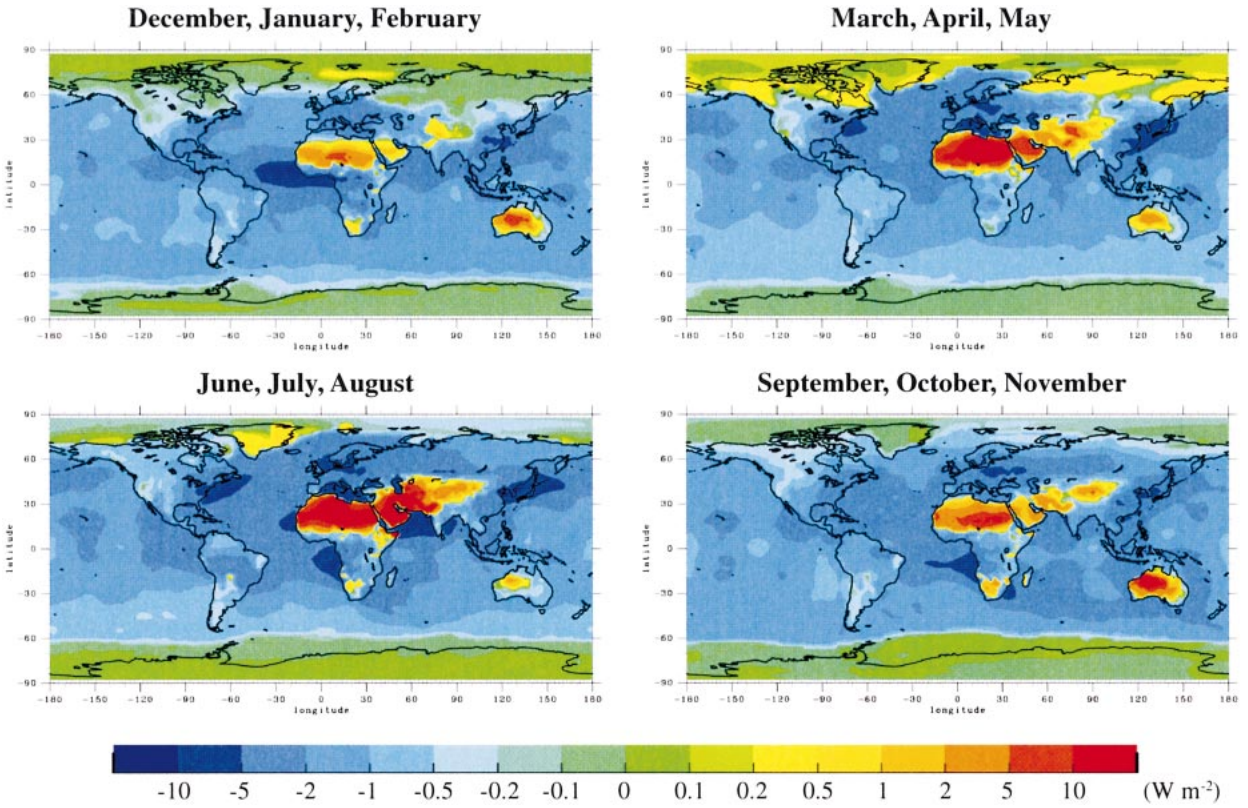

FIG. 7. Seasonal mean distributions of the simulated direct radiative forcing of a mixed polydispersion of all aerosol species, i.e., carbonaceous (OC and BC), sulfate, soil dust, and sea salt at the tropopause under clear-sky conditions in W m^{-2}.

whereas a tropical value close to 1 is from a remote ocean site. Bodhaine (1995) obtained values of about 0.97 for remote sites from nephelometers and aethalometers. The simulated single-scattering albedo is underestimated in Saharan dust regions in comparison with AERONET retrievals as mentioned in the previous paragraph. It is found, on the other hand, that biases between the simulation and observations are within retrieval errors for other AERONET sites and other measurements, though the simulated single-scattering albedo is slightly larger than the observed one over industrial regions (~0.9).

c. Simulated aerosol components

It is important to discuss which aerosol component provides the main contribution to the single-scattering albedo in a certain area. Table 5 shows AERONET and simulated single-scattering albedos, along with the contribution ratio of each aerosol species to the simulated column mass and optical thickness at selected sites of industrial, biomass burning, soil dust, and remote ocean areas. In general, the mass extinction ratio is smaller for soil dust and sea salt than for carbonaceous and sulfate aerosols because of the larger particle radius.

Table 5 shows that sulfate and carbonaceous aerosols are dominant in an industrial region for the optical thickness through the year. The good agreement between simulated and observed single-scattering albedos, which range from 0.92 to 0.96, suggests that our model assumption of the mass ratio of OC:BC is suitable for fossil fuel consumption. The dry season of southern Africa is characterized by large ratios of carbonaceous aerosols for both the simulated column mass and optical thickness. The OC:BC ratio is set at 6.92 for savanna biomass-burning sources (Table 1), so that the single-scattering albedo becomes less than 0.9. The outflow region of Saharan dust particles has a simulated column mass of soil dust larger than that of other aerosols through the year, though the ratio of carbonaceous optical thickness is also large in the Northern Hemisphere winter because of biomass burning along the Gulf of Guinea. The AERONET single-scattering albedo is, however, larger than the simulated one over soil dust regions, which was also pointed out in the previous section. Remote ocean areas without significant anthropogenic aerosols are characterized by the dominant effect of sea salt to the column mass and optical thickness and also by sulfate aerosols originating from oceanic DMS contributing to the total optical thickness. Simulated and observed values of the single-scattering albedo are therefore larger than 0.95. The Lanai, Hawaii, site occasionally has a simulated

TABLE 5. Seasonal and annual-mean values of the simulated single-scattering albedo and the ratios of each column mass and optical thickness to all aerosol components with the AERONET single-scattering albedo. CA = carbonaceous, SU = sulfate, DU = soil dust, SA = sea salt.

	Single-scattering albedo		Column mass ratio (%)				Optical thickness ratio (%)			
	AERONET	Model	CA	SU	DU	SA	CA	SU	DU	SA
Goddard Space Flight Center, Maryland (GSFC) (39°01′N, 76°52′W)										
Winter	0.92	0.95	20.2	36.8	5.6	37.4	30.4	63.7	0.5	5.4
Spring	0.93	0.95	21.0	49.3	12.9	16.8	26.0	70.1	1.3	2.6
Summer	0.96	0.96	17.8	57.0	18.8	6.4	20.9	75.0	2.7	1.4
Fall	0.94	0.94	22.5	39.3	13.7	24.5	33.7	59.8	1.7	4.8
Annual	0.94	0.95	20.4	45.6	12.7	21.3	27.8	67.1	1.6	3.5
Mongu, Zambia (15°15′S, 23°09′E)										
Winter	—	0.95	37.7	51.4	6.8	4.1	36.0	62.0	1.0	1.0
Spring	—	0.96	20.0	63.2	5.8	11.0	19.7	76.5	1.0	2.8
Summer	0.84	0.85	80.6	10.4	5.3	3.7	86.5	11.3	1.1	1.1
Fall	0.91	0.89	57.5	21.8	18.4	2.3	67.6	28.9	2.8	0.7
Annual	—	0.91	48.9	36.7	9.1	5.3	52.4	44.7	1.5	1.4
Cape Verde Island (16°43′N, 22°56′W)										
Winter	0.96	0.89	11.9	1.5	76.2	10.4	45.4	8.0	37.4	9.2
Spring	0.96	0.90	2.7	1.9	87.4	8.0	15.4	13.6	62.0	9.0
Summer	0.98	0.89	0.8	1.5	96.4	1.3	6.0	12.8	79.1	2.1
Fall	0.97	0.89	4.3	1.9	89.2	4.6	19.0	12.2	63.8	5.0
Annual	0.97	0.89	4.9	1.7	87.3	6.1	21.5	11.6	60.6	6.3
Lanai, Hawaii (20°49′N, 156°59′W)										
Winter	0.97	0.98	2.0	4.2	7.5	86.3	9.7	26.5	4.0	59.8
Spring	0.97	0.97	1.9	5.6	26.6	65.9	7.9	32.6	13.9	45.6
Summer	0.97	0.98	2.1	7.9	14.7	75.3	8.2	37.4	7.2	47.2
Fall	0.96	0.98	1.3	5.9	12.9	79.9	6.3	32.0	6.4	55.3
Annual	0.96	0.98	1.8	5.9	15.4	76.9	8.0	32.1	7.9	52.0

column mass ratio of soil dust larger in spring than in other seasons because of the outflow of Asian dust.

5. Direct radiative forcing of various aerosol species

The aerosol direct radiative forcing is calculated in this section using the simulated aerosol optical thickness and single-scattering albedo, which are in general agreement with observations except for the single-scattering albedo of soil dust as investigated in the previous section. Figure 7 shows the simulated seasonal mean radiative forcing for the direct effect of a mixture of anthropogenic and natural aerosols, which are carbonaceous, sulfate, soil dust, and sea salt at the tropopause under a clear-sky condition. The sign of the aerosol direct forcing is generally determined by the values of the single-scattering albedo and the surface albedo under the clear-sky condition. The forcing is calculated to be negative over areas of the single-scattering albedo larger than 0.85, especially around industrial and biomass-burning regions. The negative forcing in the midlatitudes of the Northern Hemisphere is larger in summer than in winter because of a larger aerosol optical thickness as explained in section 3. Seasonal mean values of the simulated maximum negative forcing are from -5 to -10 W m^{-2} in North America, Europe, and east Asia in summer. The negative forcing is also estimated to be larger than -5 W m^{-2} over the Gulf of Guinea and the tropical Atlantic in the Northern Hemisphere winter and over the southern Atlantic off southern Africa in summer. Positive forcing is, on the other hand, found over the Saharan, Near and Middle Eastern, and Chinese deserts due to a large amount of soil dust particles and the high surface albedo. Soil dust particles, however, have a negative forcing over the ocean under a clear-sky condition because of the low surface albedo. Arctic and Tibet regions are also characterized by a positive radiative forcing because of the high surface albedo of ice and snow and the long-range transport of aerosols that absorb the solar radiation such as BC and soil dust.

It has been known, on the other hand, that the aerosol direct radiative forcing is very sensitive to the structure of cloud-laden atmospheres for BC and sulfate aerosols (Haywood and Ramaswamy 1998; Liao and Seinfeld 1998). Enhanced multiple scattering increases or decreases the amount of photon interaction with aerosol particles depending on the stratification of cloud and aerosol layers. A one-dimensional radiative transfer model, which is similar to the model used in the CCSR/NIES AGCM, is used to calculate the direct radiative forcing of each aerosol species, changing the cloud water content and altitude of the cloud layer as shown in Fig. 8. The surface albedo is assumed in this calculation to be 0.07, which corresponds to the globally averaged ocean surface albedo. The forcing is negative for car-

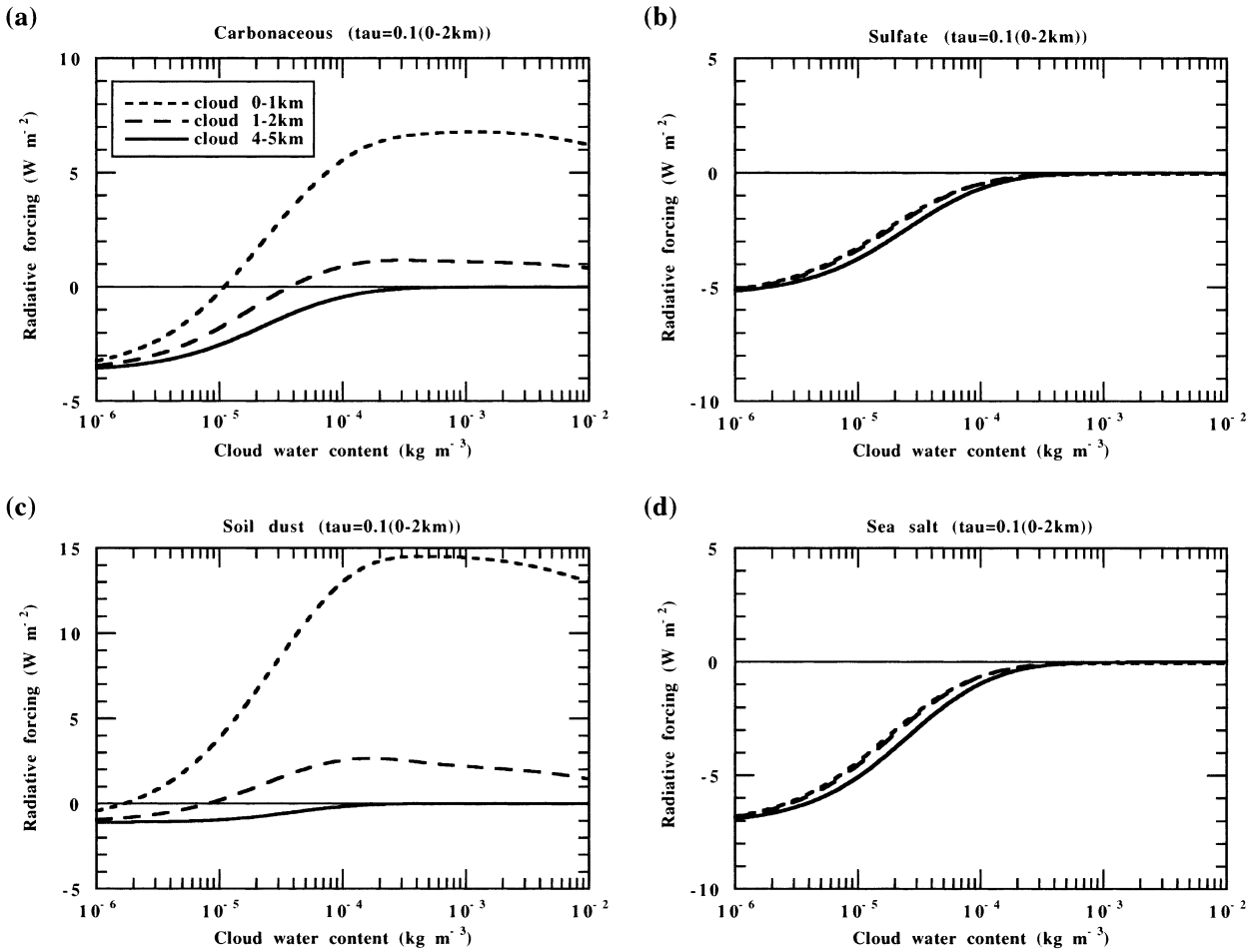

FIG. 8. Direct radiative forcing in W m^{-2} for (a) carbonaceous, (b) sulfate, (c) soil dust, and (d) sea salt aerosols as a function of the cloud water content in kg m^{-3} and the cloud layer height from 0 to 1 km (short dashed line), 1 to 2 km (long dashed line), and 4 to 5 km (solid line) assuming a vertically homogeneous aerosol optical thickness of 0.1 from 0- to 2-km height. A surface albedo of 0.07 and a cosine of solar zenith angle of 0.5 are assumed.

bonaceous and soil dust aerosols in the situation where the cloud layer is higher than the aerosol layer, whereas it becomes positive with an increase in cloud water content if the cloud layer is lower than the aerosol layer. This is because carbonaceous and soil dust aerosols absorb multiply scattered solar radiation enhanced by the cloud layer. The cloud effect in the aerosol direct forcing of soil dust was argued in detail by Quijano et al. (2000). Haywood and Ramaswamy (1998) indicated that BC near the surface tends to produce a weak positive radiative forcing due to overlying clouds. Sulfate and sea salt aerosols, that do not absorb the solar radiation significantly, produce a negative forcing even in cloudy atmospheres. The forcing value is insensitive to the altitude of a cloud layer, though it approaches 0 W m^{-2} with an increase in cloud water content. This sensitivity test suggests that an assumption of proper spatial and temporal distributions of clouds is necessary for proper estimations of not only the aerosol indirect effect but also the direct effect. It is therefore necessary to investigate whether the cloud distribution is properly simulated by the present model before studying the simulated direct radiative forcing for the whole sky. Figure 9 compares the seasonal mean cloud radiative forcing for both shortwave and longwave radiation obtained by the simulation and the Earth Radiation Budget Experiment (ERBE). The 5-yr mean ERBE data from 1985 to 1989 are used in this comparison. The figure shows that the latitudinal and seasonal patterns are similar between the simulation and the satellite retrieval and that there are no large differences except over tropical regions where the simulated cloud radiative forcing is overestimated by about 20% for the solar radiation in comparison with ERBE data.

Figure 10 shows the annual mean global distributions of the simulated direct radiative forcing by each aerosol species at the tropopause for clear-sky and whole-sky (overcast) conditions. In the mid- and high latitudes of the Northern Hemisphere, carbonaceous aerosols have positive forcing because of the high BC content origi-

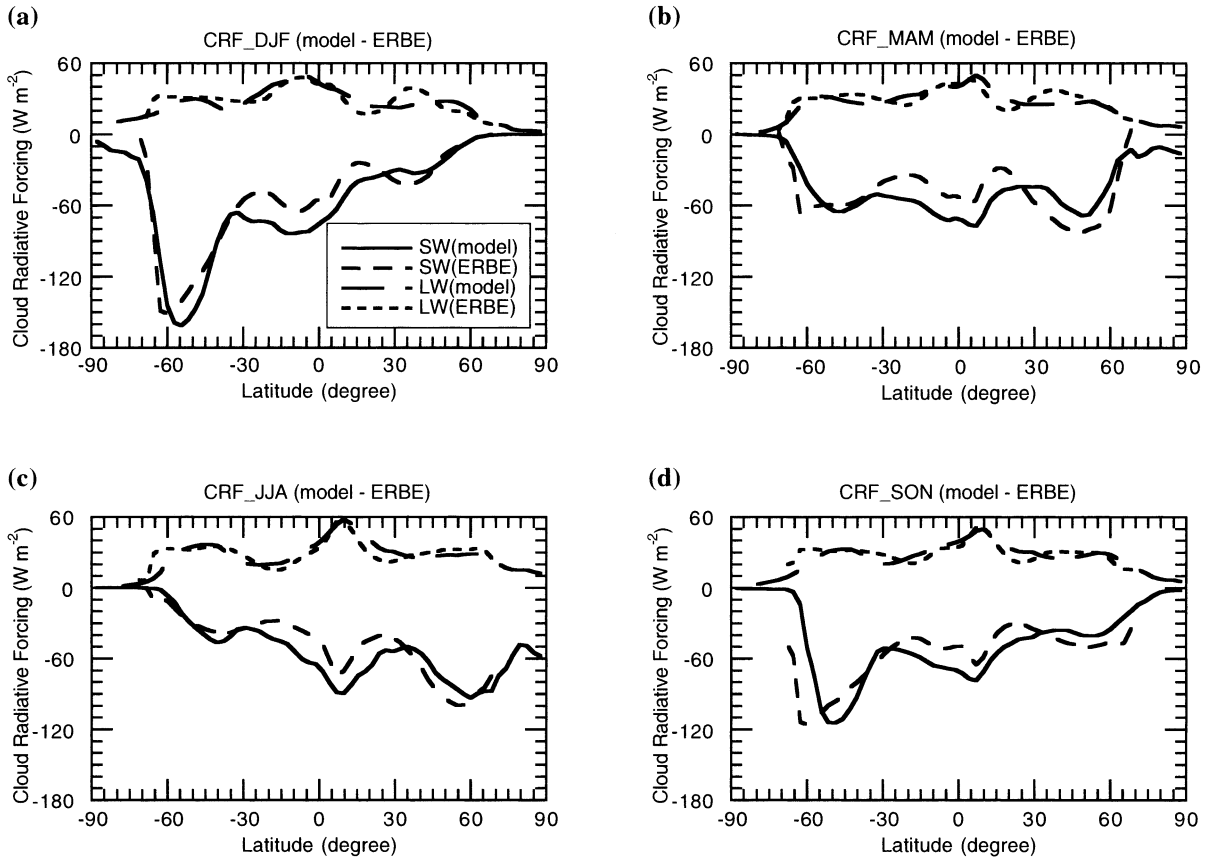

FIG. 9. Zonal mean distributions of the seasonal mean cloud radiative forcing derived from the simulation and ERBE in Northern Hemisphere (a) winter, (b) spring, (c) summer, and (d) fall.

nating from fossil fuel consumption and high surface albedo (Fig. 10a). The positive forcing is seen not only over land but also over the ocean under the whole-sky condition due to low cloud layers. The simulated annual mean forcing by carbonaceous aerosols is as large as $+1$ W m^{-2} over east Asia, Europe, and North America under the whole-sky condition. The radiative forcing of carbonaceous aerosols from biomass burning over Africa and South America can be either positive or negative. The carbonaceous positive forcing is produced over the Sahara Desert because of the high surface albedo for both clear sky and whole sky and over the southern Atlantic and the southern Indian Ocean for only whole sky because of the low altitudes of cloud layers. On the other hand, the direct radiative forcing of carbonaceous aerosols is simulated to be negative over central Africa and the Amazon even for whole sky because of the dry condition of the atmosphere when the optical thickness is large. The annual mean maximum forcing by biomass-burning carbonaceous aerosols is estimated to be about -1 W m^{-2} around biomass-burning regions over land.

Sulfate and sea salt aerosols have negative forcings globally for both clear sky and whole sky, but the forcing value is smaller for whole sky than for clear sky (Figs. 10b and 10d). This is because cloud droplets attenuate the incident solar radiation on aerosol particles. The annual mean forcing is estimated to reach -3 W m^{-2} for whole-sky conditions over industrial regions of the Northern Hemisphere due to large sulfate aerosol loading, although it has relatively small homogeneous values over the ocean with sea salt aerosols.

The positive forcing by soil dust over deserts is almost the same between clear sky and whole sky due to the high surface albedo and also due to the small cloud water path and cloud amount (Fig. 10c). On the other hand, the forcing changes from a large negative value for clear sky to a small positive value for whole sky over oceanic outflow regions because the enhanced absorption effect by clouds dominates over the enhanced reflectivity effect by the low surface albedo. The single-scattering albedo of soil dust aerosols is different among desert regions (Sokolik and Toon 1999), and the one used in this model is similar to that of the Saharan dust particles proposed by Quijano et al. (2000). It is, however, possible that absorption of the solar radiation by Saharan dust particles is excessive in the present model considering the difference in the single-scattering albedos between the simulation and AERONET (Figs.

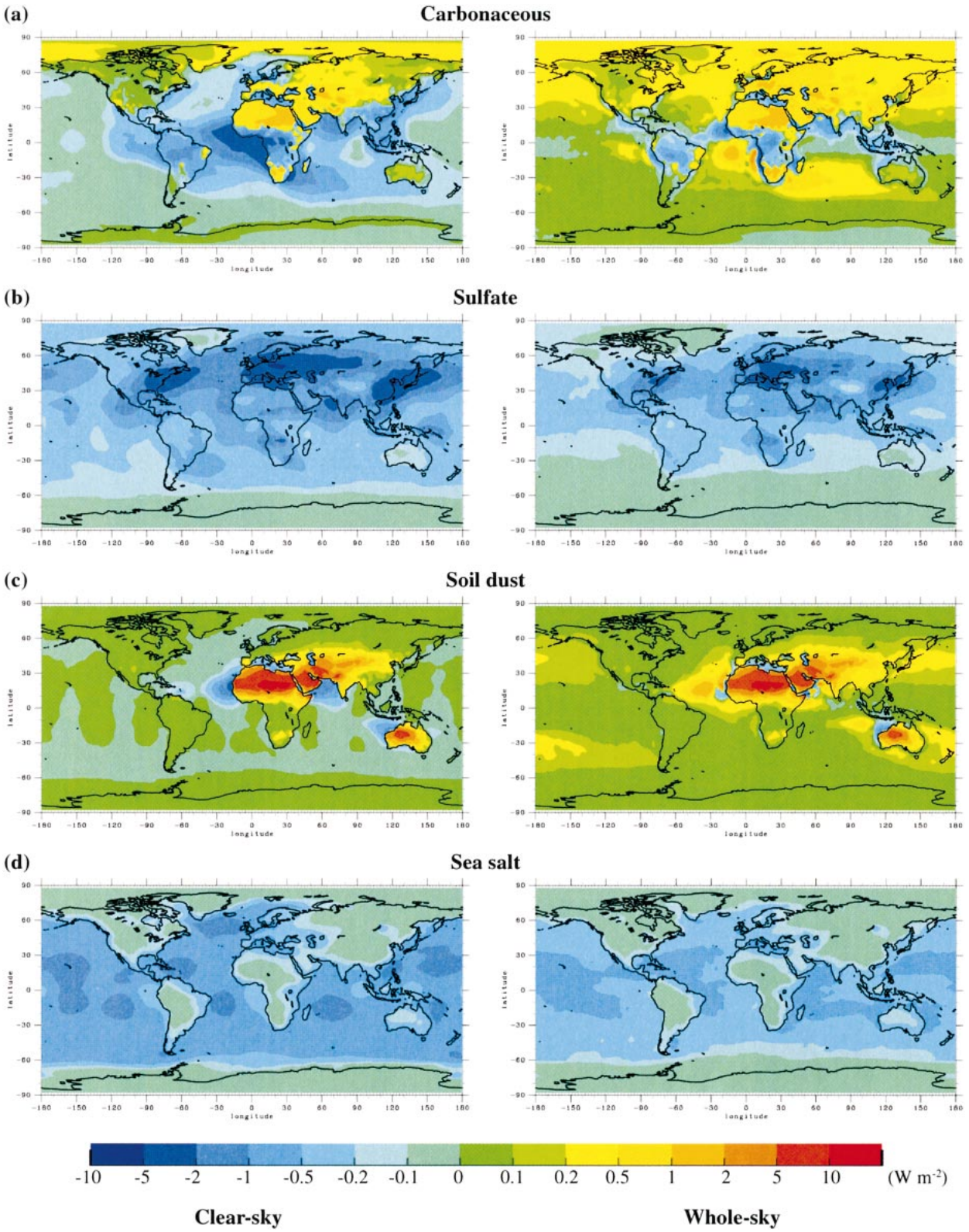

FIG. 10. Annual mean distributions of the simulated direct radiative forcing by each aerosol species of (a) carbonaceous (OC and BC), (b) sulfate, (c) soil dust, and (d) sea salt at the tropopause under clear-sky (left) and whole-sky (overcast) (right) conditions in W m^{-2}.

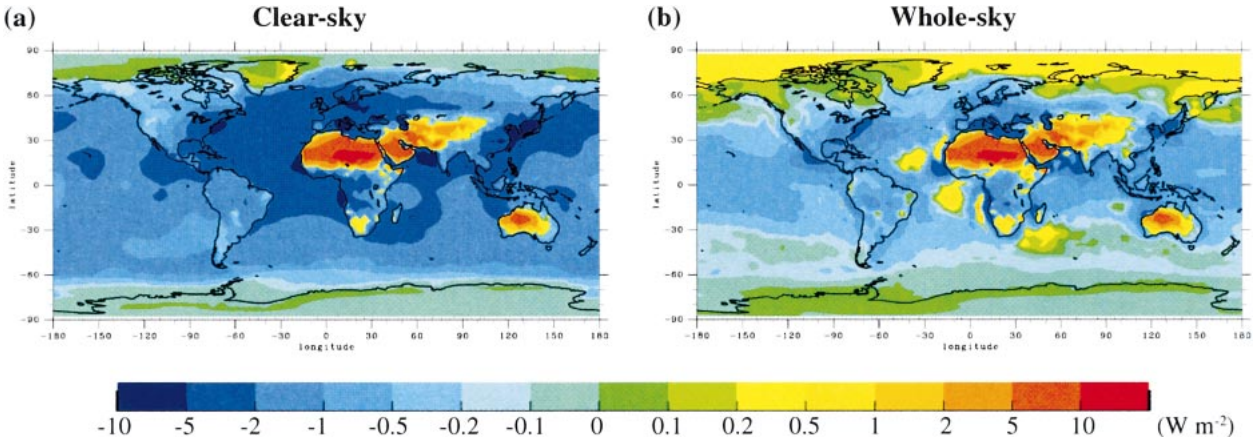

FIG. 11. Annual mean distributions of the simulated direct radiative forcing of a mixed polydispersion of all aerosol species (carbonaceous (OC and BC), sulfate, soil dust, and sea salt) at the tropopause under (a) clear-sky and (b) whole-sky (overcast) conditions in W m^{-2}.

5m–p). The simulated positive forcing may therefore be somewhat overestimated.

Table 6 lists the simulated annual mean values of the direct radiative forcing for each aerosol component at the tropopause in whole-sky and clear-sky atmospheres. In order to estimate the radiative forcing of OC and BC separately, we first perform only the OC simulation and then calculate the BC forcing as the difference between carbonaceous and OC simulations. Table 6 also includes estimates for only fossil fuel and/or biomass-burning sources for carbonaceous and sulfate aerosols. The calculated radiative forcing of carbonaceous aerosols from fossil fuel sources is +0.14 W m^{-2} (−0.05 + 0.19), which is slightly smaller than the estimate of Penner et al. (1998; Table 7). The forcing of biomass-burning carbonaceous aerosols is estimated to be close to 0 W m^{-2} (−0.16 + 0.15) for whole-sky and −0.22 W m^{-2} (−0.29 + 0.07) for clear-sky conditions. The value of the carbonaceous radiative forcing is almost the same between the Northern and Southern Hemispheres for biomass-burning sources, although it is larger for fossil fuel sources in the Northern Hemisphere. The annual global mean direct forcing by anthropogenic sulfate aerosols is calculated to be −0.32 W m^{-2} for whole sky, which is smaller than the calculations of Penner et al. (1998), Koch et al. (1999), and Kiehl et al. (2000), but similar to those of Boucher and Anderson (1995) and Feichter et al. (1997; Table 7). The differences in the estimates among studies are mainly caused by differences in the simulated aerosol column burden and the prescribed extinction efficiency depending on the relative humidity and particle size. In this respect, we have detailed comparisons of the simulated optical thickness, Ångström exponent, and single-scattering albedo with seasonal variations using the AERONET retrieval and other observations before the calculation of the direct radiative forcing. The annual mean global total burden of each aerosol species simulated by the present model is 1.91 Tg, 0.501 TgS, 21.9 Tg, and 7.23 Tg for carbonaceous, sulfate, soil dust, and sea salt aerosols, respectively. The direct radiative forcing by carbonaceous and sulfate aerosols from fossil fuel sources is

TABLE 6. Annual hemisphere and global-mean direct radiative forcing by each aerosol component at the tropopause for whole-sky (overcast) and clear-sky conditions in W m^{-2}. (NH = Northern Hemisphere, SH = Southern Hemisphere.)

	Whole sky			Clear sky		
	NH	SH	Global	NH	SH	Global
Carbonaceous (OC + BC)	+0.19	+0.06	+0.12	−0.18	−0.31	−0.24
Organic carbon (OC)	−0.29	−0.20	−0.24	−0.50	−0.40	−0.45
Fossil fuel	−0.08	−0.01	−0.05	−0.16	−0.02	−0.09
Biomass burning	−0.15	−0.17	−0.16	−0.24	−0.34	−0.29
Black carbon (BC)	+0.47	+0.26	+0.36	+0.32	+0.09	+0.21
Fossil fuel	+0.34	+0.05	+0.19	+0.24	+0.02	+0.13
Biomass burning	+0.11	+0.19	+0.15	+0.06	+0.08	+0.07
Sulfate	−0.64	−0.17	−0.40	−1.13	−0.31	−0.72
Fossil fuel	−0.55	−0.09	−0.32	−0.98	−0.16	−0.57
Soil dust	+0.60	+0.12	+0.36	+0.47	+0.05	+0.26
Sea salt	−0.32	−0.31	−0.31	−0.56	−0.63	−0.59

TABLE 7. Comparisons of the simulated global annual mean values of the aerosol direct radiative forcing in the present model with other studies.

	Direct radiative forcing (W m^{-2})
Carbonaceous (fossil fuel)	
This study	+0.14
Penner et al. (1998)	+0.16
Sulfate (anthropogenic)	
This study	−0.32
Boucher and Anderson (1995)	−0.29
Feichter et al. (1997)	−0.35
Penner et al. (1998)	−0.81
Koch et al. (1999)	−0.67
Kiehl et al. (2000)	−0.56

calculated to be −0.53 W m^{-2} (−0.09 + 0.13 − 0.57) for clear sky and −0.18 W m^{-2} (−0.05 + 0.19 − 0.32) for whole sky. The total radiative forcing of sulfate aerosols including natural sources such as DMS and volcanic SO_2 is estimated to be −0.40 W m^{-2} for whole-sky and −0.72 W m^{-2} for clear-sky conditions. In the Southern Hemisphere, the calculated radiative forcing by natural sulfate aerosols is as large as that by anthropogenic ones. The simulated direct radiative forcing of soil dust is large over arid and semiarid regions of the Northern Hemisphere, producing the annual global mean value of +0.36 W m^{-2} under whole-sky conditions. The annual mean direct forcing by sea salt aerosols is calculated to be similar between the Northern and Southern Hemispheres. The global mean direct radiative forcings by soil dust and sea salt aerosols nearly cancel each other for whole sky in the present model. As mentioned above, however, it is possible to overestimate the simulated positive forcing of soil dust in the present study. It should be noted in this regard that Tegen et al. (1996) proposed a value of +0.14 W m^{-2}.

Figure 11 shows the simulated annual mean radiative forcing of the direct effect for a mixture of anthropogenic and natural aerosols at the tropopause for the clear-sky and whole-sky conditions. The calculated radiative forcing is positive not only over desert regions but also over the ocean around Africa and the Arctic region for whole-sky conditions. The annual global mean values of the simulated direct radiative forcing of all main tropospheric aerosols are calculated to be −1.29 W m^{-2} for clear-sky and −0.24 W m^{-2} for whole-sky conditions. In midlatitude industrial regions of the Northern Hemisphere, however, the simulated forcing is negative and as large as −2 W m^{-2} even for whole-sky conditions, which is close to the global mean radiative forcing of greenhouse gases with the opposite sign (Houghton et al. 1996). The global annual mean values of the total direct radiative forcing of anthropogenic carbonaceous and sulfate aerosols, which are emitted from fossil fuel consumption and biomass burning, are calculated to be −0.19 and −0.75 W m^{-2} for whole-sky and clear-sky conditions at the tropopause, respectively. This whole-sky negative direct forcing is one-half to one-third that of the estimate of Houghton et al. (1996). It should be noted that the present model may still overestimate the magnitude of the anthropogenic negative forcing with the slight overestimation of the single-scattering albedo over industrial regions (~0.9), which is within observational error, as shown in Fig. 6.

TABLE 8. Annual hemispheric and global-mean optical thickness τ and single-scattering albedo ω with global-mean values over land and the ocean. (NH = Northern Hemisphere, SH = Southern Hemisphere.)

	τ	ω
NH	0.161	0.923
SH	0.070	0.938
Global	0.116	0.928
Land	0.134	0.906
Ocean	0.093	0.945

6. Conclusions

The aerosol optical thickness, Ångström exponent, and single-scattering albedo on a global scale were simulated using an aerosol transport model coupled with the CCSR/NIES AGCM. Simulated aerosol optical properties for the mixture of all main tropospheric aerosols, which are carbonaceous (OC and BC), sulfate, soil dust, and sea salt, have been compared with the observed optical thickness and Ångström exponent from AVHRR (Higurashi et al. 2000) and AERONET (Holben et al. 1998, 2000) and with the observed single-scattering albedo from AERONET (Dubovik and King 2000) and other measurements including seasonal variations. They are in reasonable agreement with observed values, though the single-scattering albedo from the present model is substantially lower than that from the AERONET retrieval for desert regions. The annual global mean value of the direct radiative forcing is estimated to be −0.32 W m^{-2} for anthropogenic sulfate aerosols, which had been considered to be the most dominant anthropogenic aerosols. The forcing by anthropogenic carbonaceous aerosols is, on the other hand, evaluated to be positive, +0.13 W m^{-2}. Table 8 shows hemispheric and global mean values of the aerosol optical thickness and the single-scattering albedo weighted by the optical thickness. The simulated single-scattering albedo is smaller over the Northern Hemisphere than the Southern Hemisphere and as low as 0.91 over land because of human activities. It is however 0.93 on the global scale, so that aerosol particles are calculated to cool the earth by a direct effect in the present model. In the midlatitude industrial regions of the Northern Hemisphere, the cooling effect of the aerosol direct forcing is simulated to largely cancel the warming effect by greenhouse gases, though the global mean value of the aerosol forcing is small in the present study.

There have been many past studies on estimates of

the direct radiative forcing of sulfate aerosols with chemical transport models, but they were not compared with optical observations in detail. Koch et al. (2000) roughly compared with satellite remote sensing data on the aerosol optical thickness, but they regarded sulfate as the main contributor to the aerosol optical thickness over North America, though carbonaceous aerosols are also another main contributor in industrial regions as suggested in this study. Therefore, their simulated column burden of anthropogenic sulfate aerosols was overestimated, which was 3.3 mg m^{-2} as the global annual mean, in comparison with other models. Boucher and Anderson (1995), Feichter et al. (1997), Kiehl et al. (2000), and the present study give similar values of simulated column burdens of sulfate aerosols from anthropogenic sources, which are 2.3, 2.2, 2.2, and 2.4 mg m^{-2} as the global annual mean, respectively. In spite of this agreement, the direct radiative forcing of sulfate aerosols is estimated to be -0.56 W m^{-2} by Kiehl et al. (2000); on the other hand, it was about -0.3 W m^{-2} in three other studies.

As mentioned above, Fig. 6 shows that the simulated single-scattering albedo is much smaller than the AERONET one over desert regions. Recently, Kaufman et al. (2001) indicated from the satellite remote sensing that Saharan dust absorption of solar radiation is several times smaller than the current international standards, for example, WCP-55 (1983), which is used in the present model. The simulated single-scattering albedo is, on the other hand, slightly larger than the observed one over industrial regions ($\sim$0.9) as shown in Fig. 6, though the differences are within observational error. The negative radiative forcing of anthropogenic aerosols calculated by the present model is smaller than that of the Intergovernmental Panel on Climate Change estimate, but even the present model may overestimate the negative forcing considering the differences in the single-scattering albedo between the simulation and observations.

Acknowledgments. The authors are grateful to Dr. H. Okamoto of Tohoku University for the soil dust model and useful advice; Dr. A. Numaguti of Hokkaido University for useful comments on the climate model, and we regret his death in a sudden accident; Drs. N. O'Neille, D. Tanré, R. Pinker, C. McClain, F. Lavenu, and J. V. Castle for AERONET observations.

REFERENCES

Ackerman, A. S., O. B. Toon, D. E. Stevens, A. J. Heymsfield, V. Ramanathan, and E. J. Welton, 2000: Reduction of tropical cloudiness by soot. *Science,* **288,** 1042–1047.

Bodhaine, B. A., 1995: Aerosol absorption measurements at Barrow, Mauna Loa, and the South Pole. *J. Geophys. Res.,* **100,** 8967–8975.

Boucher, O., and T. L. Anderson, 1995: General circulation model assessment of the sensitivity of direct climate forcing by anthropogenic sulfate aerosols to aerosol size and chemistry. *J. Geophys. Res.,* **100,** 26 117–26 134.

Carlson, T. N., and S. G. Benjamin, 1980: Radiative heating rates for Saharan dust. *J. Atmos. Sci.,* **37,** 193–213.

Chin, M., D. J. Jacob, G. M. Gardner, M. S. Foreman-Fowler, and P. A. Spiro, 1996: A global three-dimensional model of tropospheric sulfate. *J. Geophys. Res.,* **101,** 18 667–18 690.

Clarke, A. D., 1989: Aerosol light absorption by soot in remote environments. *Aerosol Sci. Technol.,* **10,** 161–171.

d'Almeida, G. A., P. Koepke, and E. P. Shettle, 1991: *Atmospheric Aerosols: Global Climatology and Radiative Characteristics.* A. Deepak, 561 pp.

Dubovik, O., and M. D. King, 2000: A flexible inversion algorithm for retrieval of aerosol optical properties from Sun and sky radiance measurements. *J. Geophys. Res.,* **105,** 20 673–20 696.

——, A. Smirnov, B. N. Holben, M. D. King, Y. J. Kaufman, T. F. Eck, and I. Slutsker, 2000: Accuracy assessments of aerosol optical properties retrieved from Aerosol Robotic Network (AERONET) Sun and sky radiometer measurements. *J. Geophys. Res.,* **105,** 9791–9806.

Feichter, J., U. Lohmann, and I. Schult, 1997: The atmospheric sulfur cycle in ECHAM-4 and its impact on the shortwave radiation. *Climate Dyn.,* **13,** 235–246.

Hansen, J., D. Johnson, A. Lacis, S. Lebedeff, P. Lee, D. Rind, and G. Russell, 1981: Climate impact of increasing atmospheric carbon dioxide. *Science,* **213,** 957–966.

Haywood, J. M., and V. Ramaswamy, 1998: Global sensitivity studies of the direct radiative forcing due to anthropogenic sulfate and black carbon aerosols. *J. Geophys. Res.,* **103,** 6043–6058.

Heintzenberg, J., and C. Leck, 1984: Seasonal variation of the atmospheric aerosol near the top of the marine boundary layer over Spitsbergen related to the Arctic sulphur cycle. *Tellus,* **46B,** 52–67.

Herman, J. R., P. K. Bhartia, O. Torres, C. Hsu, C. Seftor, and E. Celarier, 1997: Global distributions of UV-absorbing aerosols from Nimbus 7/TOMS data. *J. Geophys. Res.,* **102,** 16 911–16 923.

Higurashi, A., T. Nakajima, B. N. Holben, A. Smirnov, R. Frouin, and B. Chatenet, 2000: A study of global aerosol optical climatology with two channel AVHRR remote sensing. *J. Climate,* **13,** 2011–2027.

Hobbs, P. V., J. S. Reid, R. A. Kotchenruther, R. J. Ferek, and R. Weiss, 1997: Direct radiative forcing by smoke from biomass burning. *Science,* **275,** 1776–1778.

Holben, B. N., and Coauthors, 1998: AERONET—A federated instrument network and data archive for aerosol characterization. *Remote Sens. Environ.,* **66,** 1–16.

——, and Coauthors, 2001: An emerging ground-based aerosol climatology: Aerosol optical depth from AERONET. *J. Geophys. Res.,* **106,** 12 067–12 097.

Houghton, J. T., L. G. Meira Filho, B. A. Callander, N. Harris, A. Kattenberg, and K. Maskell, Eds., 1996: *Climate Change 1995: The Science of Climate Change.* Cambridge University Press, 572 pp.

Jacobson, M. Z., 2000: A physically-based treatment of elemental carbon optics: Implication for global direct forcing of aerosols. *Geophys. Res. Lett.,* **27,** 217–220.

——, 2001: Global direct radiative forcing due to multicomponent anthropogenic and natural aerosols. *J. Geophys. Res.,* **106,** 1551–1568.

Kaufman, Y. J., A. Setzer, D. Ward, D. Tanré, B. N. Holben, P. Menzel, M. C. Pereira, and R. Rasmussen, 1992: Biomass burning airborne and spaceborne experiment in the Amazonas (BASE-A). *J. Geophys. Res.,* **97,** 14 581–14 599.

——, D. Tanré, O. Dubovik, A. Karnieli, and L. A. Remer, 2001: Absorption of sunlight by dust as inferred from satellite and ground-based remote sensing. *Geophys. Res. Lett.,* **28,** 1479–1482.

Kiehl, J. T., T. L. Schneider, P. J. Rasch, M. C. Barth, and J. Wong, 2000: Radiative forcing due to sulfate aerosols from simulations

with the National Center for Atmospheric Research Community Climate Model, Version 3. *J. Geophys. Res.,* **105,** 1441–1457.
Koch, D., D. Jacob, I. Tegen, D. Rind, and M. Chin, 1999: Tropospheric sulfur simulation and sulfate direct radiative forcing in the Goddard Institute for Space Studies general circulation model. *J. Geophys. Res.,* **104,** 23 799–23 822.
Langner, J., and H. Rodhe, 1991: A global three-dimensional model of the tropospheric sulfur cycle. *J. Atmos. Chem.,* **13,** 225–263.
Liao, H., and J. H. Seinfeld, 1998: Effect of clouds on direct aerosol radiative forcing of climate. *J. Geophys. Res.,* **103,** 3781–3788.
Lin, S.-J., and R. B. Rood, 1996: Multidimensional flux-form semi-Lagrangian transport schemes. *Mon. Wea. Rev.,* **124,** 2046–2070.
——, W. C. Chao, Y. C. Sud, and K. Walker, 1994: A class of the van Leer-type transport schemes and its application to the moisture transport in a general circulation model. *Mon. Wea. Rev.,* **122,** 1575–1593.
Liousse, C., J. E. Penner, C. Chuang, J. J. Walton, H. Eddleman, and H. Cachier, 1996: A global three-dimensional model study of carbonaceous aerosols. *J. Geophys. Res.,* **101,** 19 411–19 432.
Nakajima, T., and A. Higurashi, 1998: A use of two-channel radiances for an aerosol characterization from space. *Geophys. Res. Lett.,* **25,** 3815–3818.
——, M. Tanaka, M. Yamano, M. Shiobara, K. Arao, and Y. Nakanishi, 1989: Aerosol optical characteristics in the yellow sand events observed in May, 1982 at Nagasaki—Part II. Models. *J. Meteor. Soc. Japan,* **67,** 279–291.
——, M. Tsukamoto, Y. Tsushima, A. Numaguti, and T. Kimura, 2000: Modeling of the radiative process in an atmospheric general circulation model. *Appl. Opt.,* **39,** 4869–4878.
Numaguti, A., M. Takahashi, T. Nakajima, and A. Sumi, 1995: Development of an atmospheric general circulation model. *Climate System Dynamics and Modeling,* T. Matsuno, Ed., Center for Climate System Research, University of Tokyo, 1–27.
Ohta, S., M. Hori, N. Murao, S. Yamagata, and K. Gast, 1996: Chemical and optical properties of lower tropospheric aerosols measured at Mt. Lemmon in Arizona. *J. Global Environ. Eng.,* **2,** 67–78.
Penner, J. E., C. C. Chuang, and K. Grant, 1998: Climate forcing by carbonaceous and sulfate aerosols. *Climate Dyn.,* **14,** 839–851.
Qiu, J., X. Zhou, J. Sun, Q. Xia, and J. Zhang, 1987: Simultaneous determination of the aerosol size distribution, refractive index, and surface albedo from radiance data. *Atmospheric Radiation: Progress and Process,* K. N. Liou and X. Zhou, Eds., Science Press, 550–556.
Quijano, A. L., I. N. Sokolik, and O. B. Toon, 2000: Radiative heating rates and direct radiative forcing by mineral dust in cloudy atmospheric conditions. *J. Geophys. Res.,* **105,** 12 207–12 219.
Satheesh, S. K., and V. Ramanathan, 2000: Large differences in tropical aerosol forcing at the top of the atmosphere and Earth's surface. *Nature,* **405,** 60–63.
Smirnov, A., B. N. Holben, T. F. Eck, O. Dubovik, and I. Slutsker, 2000: Cloud-screening and quality control algorithms for the AERONET database. *Remote Sens. Environ.,* **73,** 337–349.
Sokolik, I. N., and O. B. Toon, 1999: Incorporation of mineralogical composition into models of the radiative properties of mineral aerosol from UV to IR wavelengths. *J. Geophys. Res.,* **104,** 9423–9444.
Sudo, K., M. Takahashi, and H. Akimoto, 2000: Development of a photochemical GCM for the troposphere: Some experiments on the tropospheric ozone change. *Proc. Quadrennial Ozone Symp.,* Sapporo, Japan, International Association for Meteorology and Atmospheric Sciences, 181–182.
Takemura, T., H. Okamoto, Y. Maruyama, A. Numaguti, A. Higurashi, and T. Nakajima, 2000: Global three-dimensional simulation of aerosol optical thickness distribution of various origins. *J. Geophys. Res.,* **105,** 17 853–17 873.
Tanaka, M., T. Hayasaka, and T. Nakajima, 1990: Airborne measurements of optical properties of tropospheric aerosols over an urban area. *J. Meteor. Soc. Japan,* **68,** 335–345.
Tang, I. N., and H. R. Munkelwitz, 1994: Water activities, densities, and refractive indices of aqueous sulfates and sodium nitrate droplets of atmospheric importance. *J. Geophys. Res.,* **99,** 18 801–18 808.
Tegen, I., A. A. Lacis, and I. Fung, 1996: The influence on climate forcing of mineral aerosols from disturbed soils. *Nature,* **380,** 419–422.
WCP-55, 1983: Report of the experts meeting on aerosols and their climatic effects. A. Deepak and H. E. Gerber, Eds., World Meteorological Organization, 107 pp.
Yamamoto, G., and M. Tanaka, 1972: Increase of global albedo due to air pollution. *J. Atmos. Sci.,* **29,** 1405–1412.